

AMBER Force Field for Different Size Thiolate-Protected Gold Nanoclusters

*

E-mail:

Abstract

—

*To whom correspondence should be addressed

Introduction

Thiolate-protected Gold nanoclusters $\text{Au}_n(\text{SR})_m$ have been extensively studied during the past years, both experimentally and theoretically.¹ Studied clusters range in size and nature of the ligand, and exhibit interesting properties relating to, e.g., optical, electronic, catalytic and bio-compatible properties.¹ Hence, such clusters are of interest to many applications.

The ability to tune the ligand R-group to a bio-compatible group, has made these clusters interesting candidates for several biological and medical applications. While many theoretical studies of gold clusters have been conducted at the quantum mechanical level with, e.g., DFT (density functional theory), large system sizes and simulation conditions (solvent, temperature, pressure) urgent in the biological systems call for simulation techniques at classical, all-atom level able to handle systems in these sizes and capture their dynamics at sufficient time scales. Furthermore, simulations at atomistic level can reveal details on system's properties beyond experimental abilities, making simulations valuable tool in studying such systems

There have been many approaches in classical MD (molecular dynamics) and also hybrid simulations of gold clusters and gold surface systems containing various ligands and ligand free systems. For example, the development of Lennard-Jones potential parameters compatible with many traditional classical force fields for different metals by Heinz et al.² has enabled gold cluster inclusion to many different types of systems. One earlier example form of bonded potentials developed using DFT for gold-benzenedithiolate systems is presented in reference³.

Considering biological systems, gold nanoparticles have been parameterized and studied with MD in membrane systems within GROMOS united atom force field^{4–6} and within OPLS/GROMOS united atom scheme^{7,8}. Peptide adsorption and conjugation on gold surface have been studied within CHARMM^{9,10} and OPLSAA¹¹ force fields. Also other potential models have been developed to study gold-protein interactions at atomic

scale in solvent¹². Interactions of gold cluster with proteins and DNA have also been studied within AMBER force field¹³.

Molecular dynamics simulations with varying developed potentials have been utilized in studying more specifically interactions between clusters and resulting effects, e.g., in physiological conditions (within CHARMM)¹⁴ and also considering more synthesis related effects, for example gold nanoparticle aggregation¹⁵, collisions and coalescence¹⁶, structural characteristics and energetics¹⁷⁻¹⁹ and surface energetics and thermodynamical properties²⁰.

MD simulations can serve as tools in providing structures for more advanced DFT calculations, for example in studies of photochromic properties  Gold and gold cluster parameters have also been developed for the ReaxFF reactive force field²²⁻²⁴, enabling simulations containing changes in bonds and hence reaction processes. In addition QM/MM hybrid parameters have been developed for studies of gold nanoclusters²⁵ combining UFF and AMBER parameters.

The long term goal of our work is to simulate gold clusters conjugated to virus. Experimentally it has been observed that properly ligated Au₁₀₂ clusters are able to conjugate to surfaces of certain enteroviruses, echovirus 1 and coxsackievirus B3²⁶. This conjugation can be utilized in virus imaging by electron microscopy techniques and hence possibly aid in revealing structural characteristics of the virus and its functioning mechanisms.²⁶ Studying and further optimizing the mechanisms of the conjugation at atomic scale would benefit from the use of simulations alongside the experimental studies 

In this work the aim was to construct AMBER force field generalizable to different sized thiolate -protected gold clusters containing different R-groups. AMBER force field is especially designed for the simulation of proteins, and thus also the selected force field for our virus system. In the approach of this work we have selectively utilized some of the previously published parameters for different cluster systems to find a minimum set of working parameters generalizable to several different cluster sizes and able to sufficiently

maintain the DFT relaxed structures. The final parameter set adopted here was tested in 100 ns time scale simulations for $\text{Au}_{25}(\text{PET})_{18}^-$, $\text{Au}_{38}(\text{PET})_{24}$, $\text{Au}_{102}(\text{pMBA})_{44}$ and $\text{Au}_{144}(\text{PET})_{60}$, $\text{Au}_{144}(\text{pMBA})_{60}$ (PET=phenylethanethiol, pMBA=para-mercaptopbenzoic acid) clusters in different solvents. These structures are presented in figure 1. For further validation of these parameters, connections to experimental and DFT results are drawn

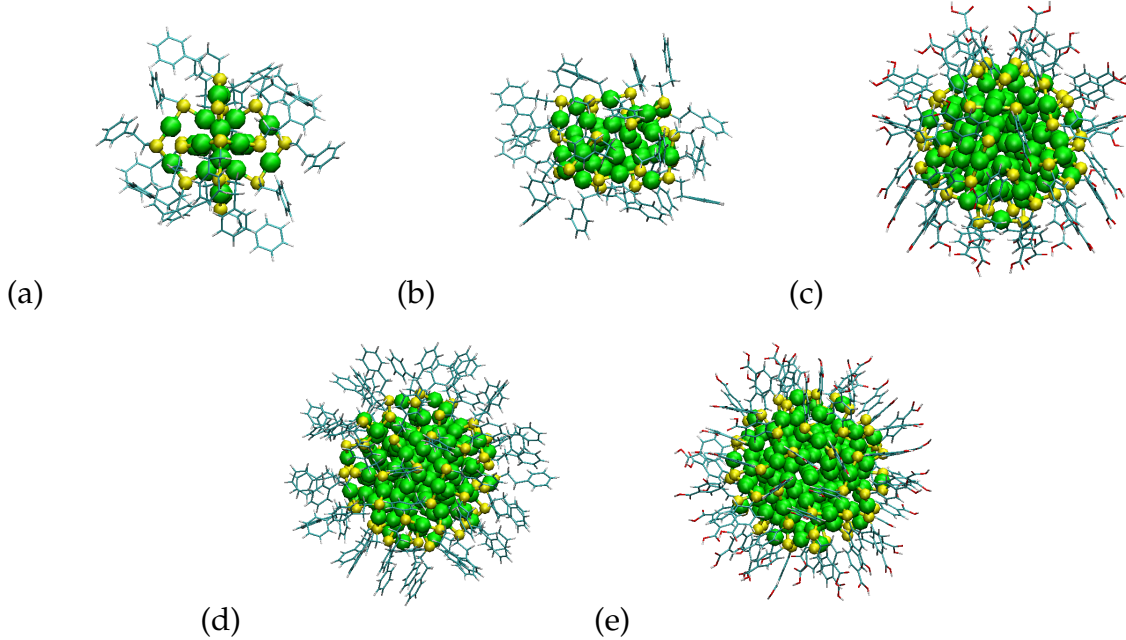


Figure 1: Clusters studied in this work. Coloring convention: green=gold; yellow=sulfur; cyan=carbon; white=hydrogen; red=oxygen. (a) $\text{Au}_{25}(\text{PET})_{18}^-$ (b) $\text{Au}_{38}(\text{PET})_{24}$ (c) $\text{Au}_{102}(\text{pMBA})_{44}$ (d) $\text{Au}_{144}(\text{PET})_{60}$ (e) $\text{Au}_{144}(\text{pMBA})_{60}$

Methods

As starting structures for all of the systems we have used DFT relaxed structures from previous works based on published crystal structures or predictions, from which the averaged equilibrium bond lengths and angles were obtained. All MD simulations were performed using Gromacs²⁷ molecular dynamics package versions 4.5.5 and 4.6.2.

Description of cluster systems

Gold nanoclusters exist in different shapes and symmetries, differing in the number of gold atoms, ligands and the chemical nature of the ligand.

Starting to view gold cluster from the core, shells arrange differently depending on the number of gold atoms. For example, Au_{25} cluster has one gold atom in the center around which 12 outer more gold atoms position to form an icosahedron. In Au_{38} the core appears less symmetric, consisting of two merged icosahedra. Larger clusters, Au_{102} and Au_{144} , contain more layers with icosahedral center and more globular overall shape. Moving outwards from the cluster core towards the surface one comes across the interface with the surface gold atoms (denoted here Au_{surf}) bonded to the sulfur atoms of the alkylthiol groups forming the protective layer over the cluster. Following the $\text{Au}_{\text{surf}}-\text{S}$ interface forms the ligand layer with the alkylthiol groups and the remaining gold atoms (denoted here Au_{lig}) that bond to two sulfur atoms and connect the alkylthiol groups forming different staple-like shapes, these are presented in figure 2.

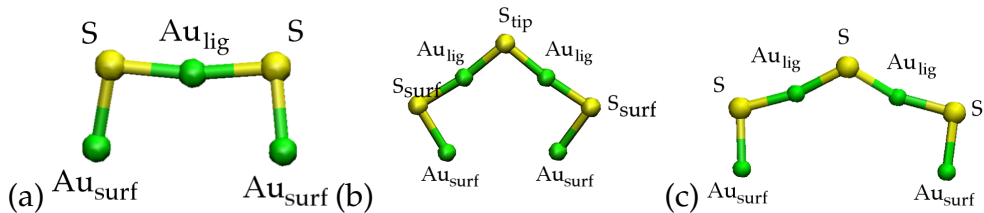


Figure 2: Different ligand unit formations related to clusters studied in this work with naming conventions and colors gold (green) and sulfur (yellow) . (a) Shows the rectangular staple formation present in Au_{38} , Au_{102} and Au_{144} clusters. The V-shape staple formation in (b) appears in Au_{25} and Au_{38} clusters and (c) in Au_{102} cluster (together with (a)). The alkylthiol groups are omitted.

Parameterization

Being developed for the simulation of proteins, AMBER99sb-ildn force field²⁸, among many other traditional force fields, does not contain parameters for gold by default. For the VDW interactions or LJ parameters we have used parameters reported in² developed

for FCC gold and compatible with (among others) AMBER force fields. By comparison, these parameters are strong compared to the existing AMBER atom types. We found, for the symmetric clusters tested in this work and similarly to references²⁹, that the resulting strong attraction in the gold core suffices to maintain the symmetry of the core structure in an MD simulation even up to high temperatures ($\gg 300$ K) without having to define any Au-Au bonds. This enables reducing the amount of bonds (constraints) in the final simulations, and solves the problem of having to define separate, system specific Au-Au bonding/constraint networks for differently shaped cluster cores³⁰. This promotes the possibility of using a more generalizable parameter set for different sized clusters.

Considering the Coulomb interaction, in this work partial charges on gold atoms in all systems were approximated to 0. Bader analysis²⁹ revealed relatively small charges on Au atoms compared to those of ligand atoms. The scheme for 0 charged Au atoms has also been adopted in references^{10,25}.

For the bonded parameters, bond lengths and angles, between Au and S atoms the aim was to find a minimum set of parameters sufficient to maintain the shape of the staples (and the core) in simulations. The equilibrium bond lengths and angles were averaged from DFT relaxed structures for each system²⁵. The harmonic force constant for the Au_x-S bonds was adopted from²⁵. This constant is generally about one order of magnitude smaller than those readily existing in AMBER. The harmonic angle force constants for different combinations of $\text{Au}_x-\text{S}-\text{Au}_x$ were taken from reference⁷, which are in general comparable to those pre-existing in AMBER. To keep the staple more rigid, the force constant for angle $\text{S}-\text{Au}_{\text{lig}}-\text{S}$ was also adopted from reference⁷. The value for this is about 3 times larger than those pre-existing in AMBER, allowing better retaining of the staple like shape. For $\text{Au}_x-\text{S}-\text{C}_x$ angle force constants those presented in reference²⁵ were utilized. These are in general smaller compared to those pre-existing in AMBER, allowing for improved dynamics of the ligand shell.

For the parameterization of alkylthiol groups, in this work pMBA and PET (figure 3),

standard atom types pre-existing in AMBER99sb-ildn were used. For the missing bond and angle types, mainly those containing sulfur, force constant of similar bonds pre-existing in AMBER were used, and the equilibrium length/angle averaged from the DFT relaxed structures

For the partial charges of the alkylthiol groups RESP charge fitting procedure recommended for AMBER was performed with Ambertools12³³ package. The charges were derived for systems of type Au₂(PET)₂ and Au₂(pMBA)₂, similarly to reference. The structures Au₂(PET)₂ and Au₂(pMBA)₂ were first geometry optimized using Gaussian09³⁴ with B3LYP functional and LANL2DZ basis set with W06 density fitting basis³⁵, followed by an ESP calculation with radius for Au=1.7. The resulting ESP potential was used in a 2-stage RESP fit within Ambertools package. The final fittings were done with constraining charges on Au atoms to 0. For the pMBA ligand partial charges were fitted both for the protonated and deprotonated structures. For the Au₂₅ both neutral and anionic systems were defined; for the anionic version the charges were fitted so that the overall charge in the full cluster would be -1 with charge Au still 0. All charges obtained from RESP were compared to similar pre-existing residue parts in AMBER and no drastic discrepancies were observed.

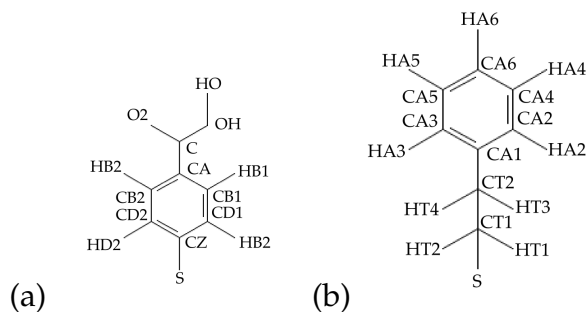


Figure 3: Alkylthiol ligands and naming conventions used in this work (a) pMBA= para-mercaptobenzoic acid and (b) PET= phenyl-ethanethiol.

Model validation

For testing of the parameters all clusters were simulated in solvent up to time scales in order of 100 ns to establish the stability. In all simulations md integrator with time step of 2 fs, PNElectrostatics and velocity-rescale thermostat (298.15 K) and berendsen barostat (1 bar) were used with all bonds constrained with LINCS constraint algorithm. Clusters Au₂₅(PET)₁₈, and Au₃₈(PET)₂₄ were simulated in chloroform. For the Au₂₅(PET)₁₈⁽⁻⁾ cluster both charged and neutral form were simulated. Clusters Au₁₀₂(pMBA)₄₄ and Au₁₄₄(pMBA)₆₀ were simulated in TIP3P water. For Au₁₀₂(pMBA)₄₄ cluster we tested systems with all pMBA groups either protonated or deprotonated. For the deprotonated case, neutralizing counter ions (Na) were added to the simulation. For Au₁₄₄(pMBA)₆₀ cluster only fully protonated case was tested. Au₁₄₄(PET)₆₀ cluster was simulated in dichloromethane. The solvent (GAFF³⁶) parameters and structures were obtained from Virtualchemistry website^{37,38} for chloroform and dichloromethane. Prior to simulations each system was energy minimized and equilibrated under NVT (100 ps) and NPT (100 ps).

To provide more justification of the parameters diffusion coefficients were computed from simulations to compare with experimental data in reference³⁹ available for Au₂₅, Au₃₈ (in chloroform) and Au₁₄₄ (in dichloromethane) clusters with PET ligand. Prior to sampling simulations each system (one cluster in cubic simulation box) was energy minimized and equilibrated under NVT and then NPT for a total of 2.1 ns. For better statistics averaging scheme similar to that proposed in reference⁴⁰ was used, so that for each system 20 5 ns sampling simulations (NPT, 298.15 K, 1 bar) with random initial velocities were performed. To account for the finite size effects, the simulations for each of the three cluster systems were repeated in three different sized cubic boxes. Cluster diffusion coefficients $D_{cluster}$ in each system and box size were calculated from the Einstein

relation (in 3 dimensions):

$$D_{cluster} = \lim_{t \rightarrow \infty} \frac{\langle ||\mathbf{r}_i(t) - \mathbf{r}_i(0)||^2 \rangle}{6t} \quad (1)$$

where $\langle ||\mathbf{r}_i(t) - \mathbf{r}_i(0)||^2 \rangle$ denotes the mean square displacement (*MSD*). The Stokes-Einstein equation relates the hydrodynamic radius r of a spherical particle in homogeneous solution to its diffusion coefficient by

$$r = \frac{k_B T}{6\pi D_{cluster} \eta} \quad (2)$$

where η is the viscosity of the solvent. Here we used *MSD* averaged from 20 simulations. Linear fitting to equation 1 was done between 0.5-4.5 ns and error estimated as the difference between fits of 0.5-2.5 ns and 2.5-4.5 ns. Diffusion coefficient in an infinite dilution was estimated from the intercept of an error weighted linear fit to box size dependent diffusion coefficient data.

Another validation against experimental result, the experimental crystal structure of $\text{Au}_{102}(\text{pMBA})_{44}$ ⁴¹ was simulated to assure the maintenance of the experimental crystal structure when simulated in crystallization conditions. For this purpose a $\text{Au}_{102}(\text{pMBA})_{44}$ crystal of 72 clusters was constructed and solvated in mixture of water/methanol/NaCl/-NaOAc approximately corresponding to amounts reported in the experimental crystallization data. The methanol (GAFF) parameters were obtained from Virtualchemistry and sodium acetate parameterized utilizing Ambertools12. In the simulation the structure was energy minimized, followed by 1 ns solvent relaxation (Cluster's non-hydrogen atoms restrained, NVT 200 K), and then without restraints: 1 ns NVT at 298.15 K and 1 ns NPT at 298.15 K, 1 bar. For the production the crystal was simulated under NPT (298.15 K, 1 bar) for 100 ns. All pMBA groups were kept protonated.

In addition to experimental data, comparisons were made against DFT calculations. To this end comparisons concerned the energy profiles of ligand flipping in some of the

cluster staple structures. This was concerned due to relatively excessive ligand flipping observed in the first simulations. The energy barriers for ligand flipping in two staple forms, the ones present in $\text{Au}_{25}(\text{PET})_{18}$ and $\text{Au}_{102}(\text{pMBA})_{44}$ clusters, were studied with DFT using constrained relaxation. The flipping trajectory was rerun in an MD simulation with the proposed force field parameters and the resulting energy barriers were compared.

In addition comparisons of dynamics and structural changes in $\text{Au}_{25}\text{PET}_{18}^-$ cluster in MD simulations of different time scales were compared to picosecond scale vacuum dynamics of an MD/DFT simulation, with 0.5 ps trajectory for $\text{Au}_{25}\text{PET}_{18}^-$ structure and previous results⁴² for $\text{Au}_{25}\text{H}_{18}^-$ of 10 ps trajectory. The structural changes were compared by studying distributions of non-constrained atomic distances and angles, in addition to root mean square deviations and displacements.

Results and discussion

Parameters

In this section the complete set of parameters we found to be sufficient to enable retaining the shape of the gold core and staple structures in simulations up to 100 ns time scale in solvent are summarized. The non-bonded parameters, LJ σ and ϵ and partial charges q from RESP fit, with atom types and names are presented in table 1. The LJ parameters for Au are obtained from², all the rest are those pre-existing in AMBER99sb-ildn²⁸ and presented for completion and indicating the atom types used for the ligands. The bonded parameters for bonds and angles (harmonic), force constants k_b and k_θ and equilibrium values d_{eq} and θ_{eq} , are presented in table 2. The parameters within ligand (PET or pMBA) which are automatically determined by the selected atom types are omitted. The missing force constants for the ligands were taken from similar bonds, angles or dihedrals pre-existing in AMBER99sb-ildn (presented and indicated with *).

Table 1: Non-bonded parameters for all atom types used in simulations. Partial charges for deprotonated pMBA, and PET ligand to obtain negatively charged $\text{Au}_{25}(\text{PET})_{18}^-$ cluster are presented in parentheses () .

Atom name	Atom type	σ (nm)	ϵ (kJ/mol)	q (e)
Au	Au	0.2629	22.1330	0
pMBA				
C	C	0.0339967	0.359824	0.6641 (0.7245)
CZ	CA	" "	" "	0.0689 (0.0827)
CD ₁	CA	" "	" "	-0.0557 (-0.0707)
CB ₁	CA	" "	" "	-0.1604 (-0.1985)
CA	CA	" "	" "	-0.0029 (0.0463)
CB ₂	CA	" "	" "	-0.1604 (-0.1985)
CD ₂	CA	" "	" "	-0.0557 (-0.0707)
HD ₁	HA	0.259964	0.06276	0.1191 (0.1000)
HB ₁	HA	" "	" "	0.1596 (0.1458)
HD ₂	HA	" "	" "	0.1191 (0.1000)
HB ₂	HA	" "	" "	0.1596 (0.1458)
HO	HO	0.000000	0.000000	0.4619 (-)
O ₂	O	0.295992	0.87864	-0.5237 (-0.7282)
OH	OH	0.306647	0.880314	-0.6417 (-0.7282)
S	S	0.356359	1.04600	-0.1518 (-0.3504)
PET				
CA ₁	CA	0.339967	0.359824	0.0298 (0.0267)
CA ₂	CA	" "	" "	-0.1582 (-0.1613)
CA ₃	CA	" "	" "	-0.1582 (-0.1613)
CA ₄	CA	" "	" "	-0.1799 (-0.1829)
CA ₅	CA	" "	" "	-0.1799 (-0.1829)
CA ₆	CA	" "	" "	-0.0932 (-0.0964)
CT ₁	CT	0.339967	0.45773	-0.0026 (-0.0057)
CT ₂	CT	" "	" "	-0.1101 (-0.1132)
HT ₃	H ₁	0.247135	0.0656888	0.0773 (0.0742)
HT ₄	H ₁	" "	" "	0.0773 (0.0742)
HA ₂	HA	0.259964	0.06276	0.1468 (0.1437)
HA ₃	HA	" "	" "	0.1468 (0.1437)
HA ₄	HA	" "	" "	0.1469 (0.1438)
HA ₅	HA	" "	" "	0.1469 (0.1438)
HA ₆	HA	" "	" "	0.1287 (0.1257)
HT ₁	HC	0.264953	0.065888	0.0903 (0.0872)
HT ₂	HC	" "	" "	0.0903 (0.0872)
S	S	0.356359	1.04600	-0.1990 (-0.2021)

Table 2: Bonded parameters. Equilibrium bond lengths d_{eq} and angles θ_{eq} are presented for each system in order $\text{Au}_{25}(\text{PET})_{18}$, $\text{Au}_{38}(\text{PET})_{24}$, $\text{Au}_{102}(\text{pMBA})_{44}$, $\text{Au}_{144}(\text{PET})_{60}$, $\text{Au}_{144}(\text{pMBA})_{60}$.

bond	k_b (kJ mol ⁻¹ nm ⁻²)	d_{eq} (nm)
$\text{Au}_{\text{surf}}-\text{S}$	62730 ²⁵	0.244/0.238 & 0.236/0.246/0.245/0.239
$\text{Au}_{\text{lig}}-\text{S}$	62730 ²⁵	0.235/0.230/0.236/0.234/0.230
$\text{CA}-\text{S}$	198321.6*	0.175
$\text{CT}-\text{S}$	99113.0 ²⁵	0.184
angle	k_θ (kJ mol ⁻¹ rad ⁻²)	θ_{eq} (°)
$\text{Au}_{\text{surf}}-\text{S}-\text{Au}_{\text{lig}}$	460.240 ⁷	91.7/94.0 & 88.0/87.0 & 100.6/86.0/91.7
$\text{S}-\text{Au}_{\text{lig}}-\text{S}$	1460.240 ⁷	174.0/170.0/172.0 & 164.1/177.0/177.0
$\text{Au}_{\text{lig}}-\text{S}-\text{Au}_{\text{lig}}$	1460.240 (460.24) ⁷	100.0/99.0/(119.2)//-/-
$\text{Au}_{\text{surf}}-\text{S}-\text{C}$	146.370 ²⁵	109.0/107.0/114.0/109.0/119.0
$\text{Au}_{\text{lig}}-\text{S}-\text{C}$	146.370 ²⁵	104.0/106.0/108.0/104.0/112.0
$\text{CA}-\text{C}-\text{OH}$	585.76*	112.0
$\text{CA}-\text{C}-\text{O}$	585.76*	126.0
$\text{CA}-\text{CA}-\text{S}$	418.40*	120.0
$\text{S}-\text{CT}-\text{HC}$	418.40*	107.0
$\text{H}_1-\text{CT}-\text{CA}$	418.40*	109.0
dihedral	(kJ/mol)	ψ
X-X-CA-S	4.60240*	180.00*
C-CA-CA-CA	4.60240*	180.00*

In addition to bonded parameters presented in table 2, an improper dihedral potential (type 2 in Gromacs) was used with atoms $\text{C}-\text{Au}_{\text{lig}}-\text{Au}_{\text{surf}}-\text{S}$ to restrict excessive flipping of PET or pMBA groups in simulations. The parameters for this potential were directly adopted from Gromos96FF with angle of 35.26439° and force constant 334.841 kJ mol⁻¹ rad⁻².

Test simulations

100 ns test simulations in solvent showed no visual breaking of cluster symmetries, defined by the core gold atoms, in any of the clusters simulated in this work, in spite of the lack of

bonds (constraints) between all the gold atoms. The ligand shell appeared dynamic in all of the simulations. The rectangular staple shapes were retained well in the simulations of the larger clusters, whereas the V-shaped staple shape present in $\text{Au}_{25}(\text{PET})_{18}^{(-)}$ (and $\text{Au}_{38}(\text{PET})_{24}$) clusters was clearly more distorted and  during the simulation from visual inspect, even more so in the $\text{Au}_{25}(\text{PET})_{18}^{(-)}$ cluster. This distortion is depicted in figure 4.

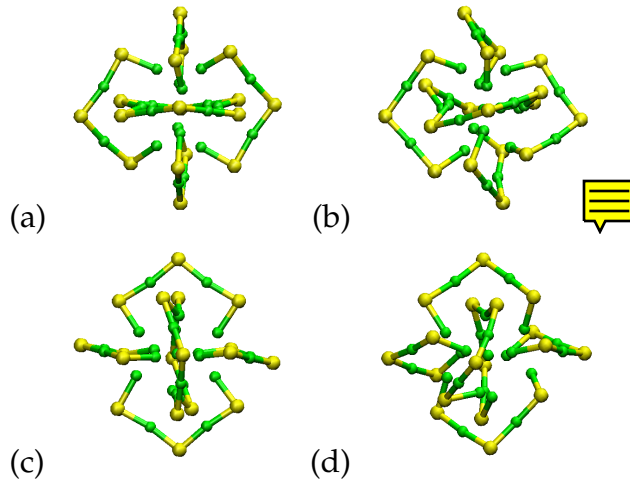


Figure 4: Staple distortion in the simulation of $\text{Au}_{25}(\text{PET})_{18}^{(-)}$. (a), (c) show the original structure and (b), (d) the structure after 100 ns simulation.

The dynamical features of different clusters were studied in more detail by looking at the gyration radius (indication of the cluster's size and shape) and root mean square deviations. These are presented in figures 5 and 6.

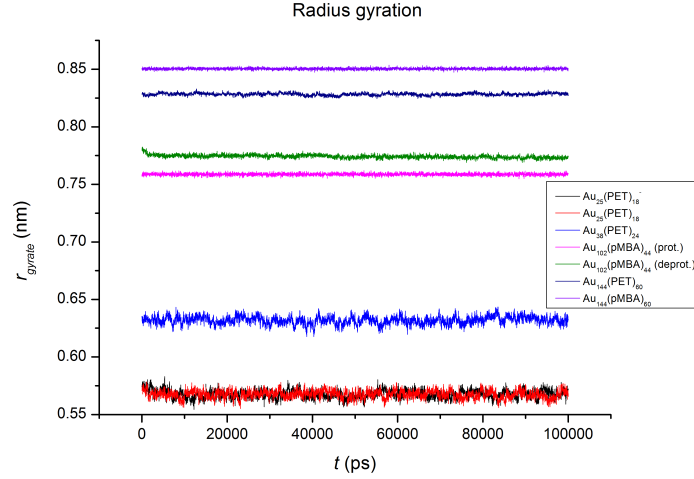


Figure 5: Gyration radii.

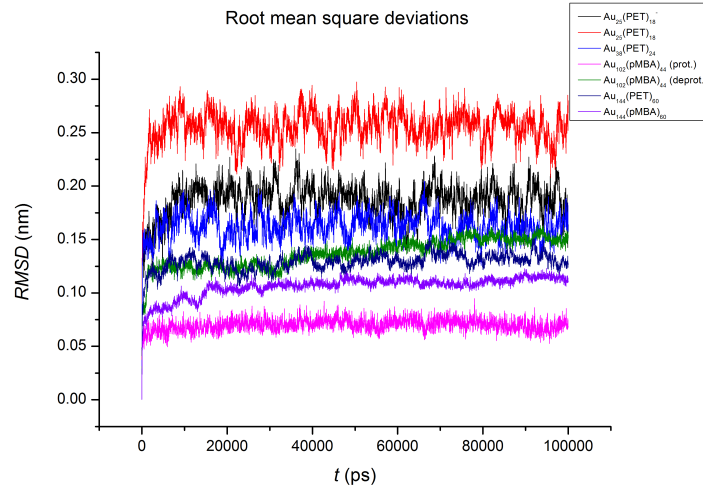


Figure 6: Root mean square deviations.

Looking at the gyration radius, figure 5 shows larger fluctuations for the smaller $\text{Au}_{25}(\text{PET})_{18}^{(-)}$ and $\text{Au}_{38}(\text{PET})_{24}$ clusters in comparison to the ones with >100 Au atoms. This could be explained by the differences in the staple shapes, and hence more empty space around each ligand in these smaller clusters enabling more excessive folding and refolding. Similar trend is seen in the root mean square deviations, figure 6, both in the magnitude of the deviations and also the fluctuations that appear larger for these small

clusters. The $\text{Au}_{25}(\text{PET})_{18}^{(-)}$ clusters exhibit the largest deviations, probably due to the large empty space around the cluster enabling more free movement of ligands compared also to the $\text{Au}_{38}(\text{PET})_{24}$ cluster. Furthermore, there also appears difference in the deviations of the charged and neutral $\text{Au}_{25}(\text{PET})_{18}^{(-)}$ clusters, with the neutral one exhibiting larger deviations. These differences probably relate to the different partial charges in the PET ligand for the charged and neutral state. Considering larger clusters, the deviations in $\text{Au}_{144}(\text{PET})_{60}$ appear minutely larger compared to $\text{Au}_{144}(\text{pMBA})_{60}$. There also appears difference for the $\text{Au}_{102}(\text{pMBA})_{44}$ cluster depending on the protonation state, with the fully protonated cluster exhibiting smaller deviation. This could be related to presence of ions in the simulation of the fully deprotonated cluster, and hence difference in solvent conditions.

On the whole, the 100 ns time scale simulations in solvent did not reveal any instabilities in the structures for any of the clusters, and the cluster shapes were retained while the ligand shell was dynamic. Whether the folding or distorting of the staples in the smaller clusters is too excessive or physically sound will be discussed in more detail in the further sections.



Diffusion coefficients

Diffusion coefficients calculated from Einstein relation (equation 1) using the averaging scheme described in the previous section for each cluster system and box size (described here by the cubic box side length L) are presented in table 3. Extrapolation to infinite box size was approximated from error weighted linear fit to $1/L, D_{\text{cluster}}$ data. These results are presented with standard errors in bold. Experimental results taken from³⁹ are presented for comparison.

Table 3: Diffusion coefficients calculated from Einstein relation and averaged from 20 separate 5 ns simulations. Errors estimated from difference between fits of 0.5-2.5 ns and 2.5-4.5 ns. Final result in infinite box size estimated from error weighted 3 point linear fit to results for different L . Experimental diffusion coefficients³⁹ are presented from comparison (Reported experimental standard deviation <8%)

System	L (nm)	D_{cluster} ($10^{-5}\text{cm}^2/\text{s}$)	$D_{\text{experimental}}$ ($10^{-5}\text{cm}^2/\text{s}$)
$\text{Au}_{25}(\text{PET})_{18}$	2.32	0.015 ± 0.001	
$\text{Au}_{25}(\text{PET})_{18}$	4.13	0.213 ± 0.02	
$\text{Au}_{25}(\text{PET})_{18}$	6.07	0.367 ± 0.06	
$\text{Au}_{25}(\text{PET})_{18}$	∞	0.479 ± 0.04	0.484
$\text{Au}_{38}(\text{PET})_{24}$	2.55	0.015 ± 0.001	
$\text{Au}_{38}(\text{PET})_{24}$	4.58	0.118 ± 0.04	
$\text{Au}_{38}(\text{PET})_{24}$	6.64	0.287 ± 0.03	
$\text{Au}_{38}(\text{PET})_{24}$	∞	0.426 ± 0.08	0.374
$\text{Au}_{144}(\text{PET})_{60}$	3.46	0.030 ± 0.003	
$\text{Au}_{144}(\text{PET})_{60}$	5.90	0.185 ± 0.002	
$\text{Au}_{144}(\text{PET})_{60}$	8.35	0.252 ± 0.04	
$\text{Au}_{144}(\text{PET})_{60}$	∞	0.405 ± 0.001	0.356

In general, the trend of decreasing diffusion coefficient with increasing cluster size observed in the experiment is reproduced in the simulations. This is in a way to be expected, since the hydrodynamic radius of a spherical particle is inversely proportional to the diffusion coefficient via equation 2. For the $\text{Au}_{25}(\text{PET})_{18}$ cluster the calculated diffusion coefficient appears smaller and for $\text{Au}_{38}(\text{PET})_{24}$ and $\text{Au}_{144}(\text{PET})_{60}$ larger than the experimental one. Considering the relatively large errors, experimental values are found within the error ranges for the calculated diffusion coefficients for $\text{Au}_{25}(\text{PET})_{18}$ and $\text{Au}_{38}(\text{PET})_{24}$ clusters (relative errors around 8% and 18%, respectively). For $\text{Au}_{144}(\text{PET})_{60}$ cluster the standard error in turn appears ~~especially~~ small and the experimental value is not included in this error range.

The differences between calculated and experimental diffusion coefficients, and the relatively large errors in the calculated ones, can be related to too low statistic in the simulation procedure, especially considering only three different system sizes for finite

size effect removal. In addition the solvent parameters may have an effect, e.g., in the experiment reported solvents were CDCl_3 and CD_2Cl_2 whereas in simulations we have technically used parameters for CHCl_3 and CH_2Cl_2 . For example, differences in solvents' viscosities could affect the solute diffusion coefficient according to equation 2.

The cluster parameters also affect the diffusion coefficients. With the hydrodynamic radius relating to the diffusion coefficient via equation 2, too small/large diffusion coefficient could indicate too large/small hydrodynamic radius and hence too low/excessive folding of the ligand. Qualitatively however, the calculated diffusion coefficients correspond well to the experimental values. In that sense also the hydrodynamic radii and further the ligand folding and even the staple distortion, in the extent observed in the simulation, could be justified.

Crystal simulation

For simulation of the crystal structure of $\text{Au}_{102}(\text{pMBA})_{44}$ ⁴¹, figure 7 shows comparisons of the crystal structure constructed from the experimental data and the averaged structure from the 100 ns production simulation from different directions.

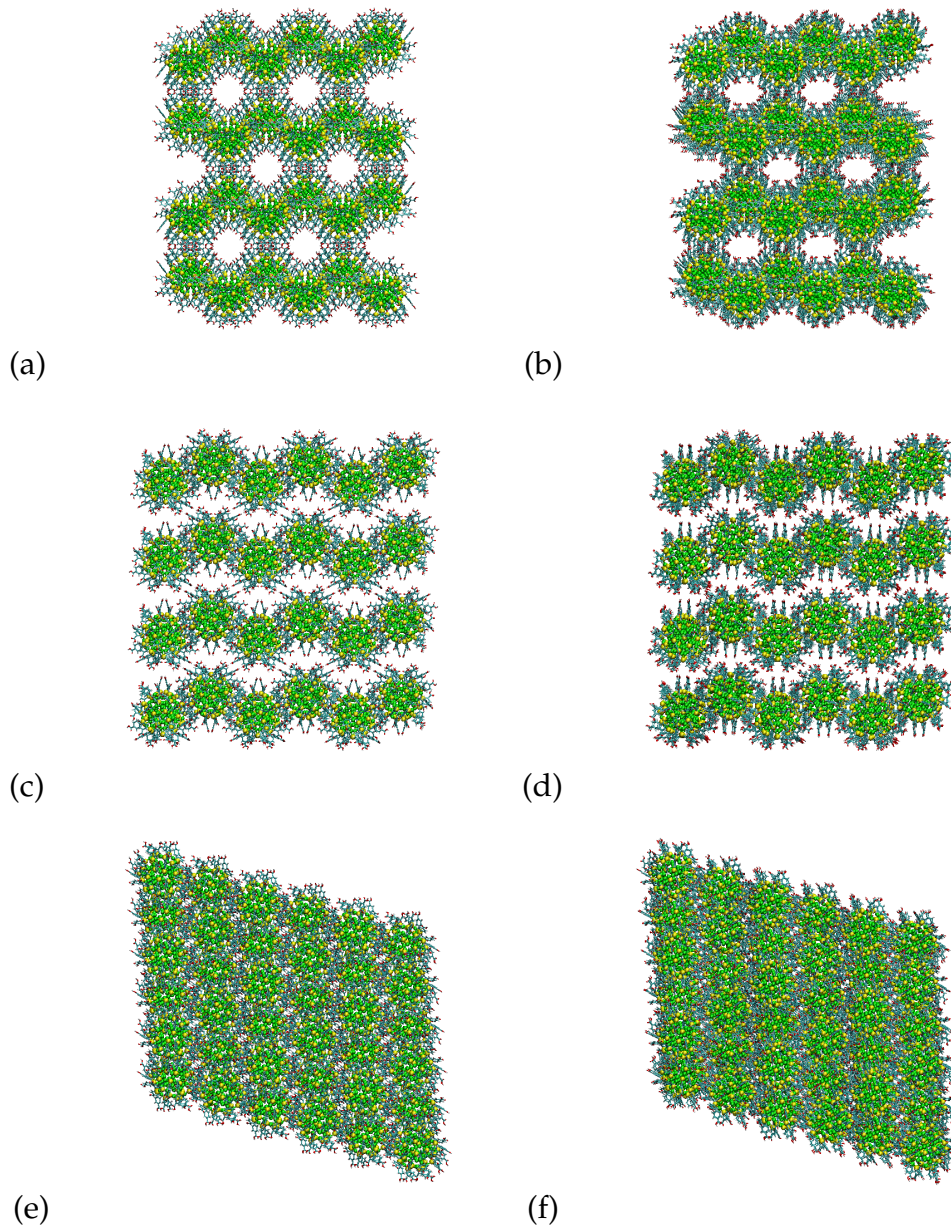


Figure 7: Simulation of 72 cluster crystal of $\text{Au}_{102}(\text{pMBA})_{44}$. (a), (c), (e) show the experimental crystal structure and (b), (d), (f) the averaged structure from 100 ns production simulation.

Visually the most significant change can be seen in direction (a) vs. (b) where the pores in the crystal are distorted or compressed to some extent. This could be related to the possibly improper filling of these pores with the solvent in the start of the simulation. In addition, unoptimized protonation of all the pMBA groups in the simulation could

result in changes of the hydrogen bonds between the clusters and hence the overall crystal structure. In the directions (c) vs. (d) and (e) vs. (f) the changes or distortions are not as emphasized from the visual [§]ect.

In addition to system in solvent mimicking the crystallization conditions, a system solvated in pure TIP3P water was also tested. For this a compressed water box was used to obtain sufficient solvent content in the unit cell [§]he results from water solvated simulations were clearly [§]s successful in comparison to that in mimic solvent. In water solvated simulations the visual distortions compared to the original crystal structure in all directions were more emphasized. Looking into root mean square deviations of the crystals compared to the original crystal structure, the mimic solvated system converges fast to the approximate value in order of 0.1 nm, whereas crystal in the water solvated system keeps increasing throughout the 50 ns simulation approaching >0.6 nm. Mapping changes in the cluster center of mass distances in comparison to the crystal structure shows maximum changes of 0.16 nm and 0.9 nm for the mimic and water solvated systems, respectively.

In spite of the short simulation time and ambi[§]us results, it can be noted that the crystal structure is maintained relatively well in the simulation in the mimic solvent, indicating that there are at least no severe discrepancies in the cluster parameters. Interestingly the crystal structure is not maintained as well when simulated in the 'wrong' solvent, promoting the simulation's ability to reproduce an experimental result.

Potential profiles

For comparison of the barrier profiles, DFT flipping trajectory was rerun in an MD simulation with the staple parameters (excluding the chirality flipping restricting potential). The resulting energy barriers are presented in figure 8.

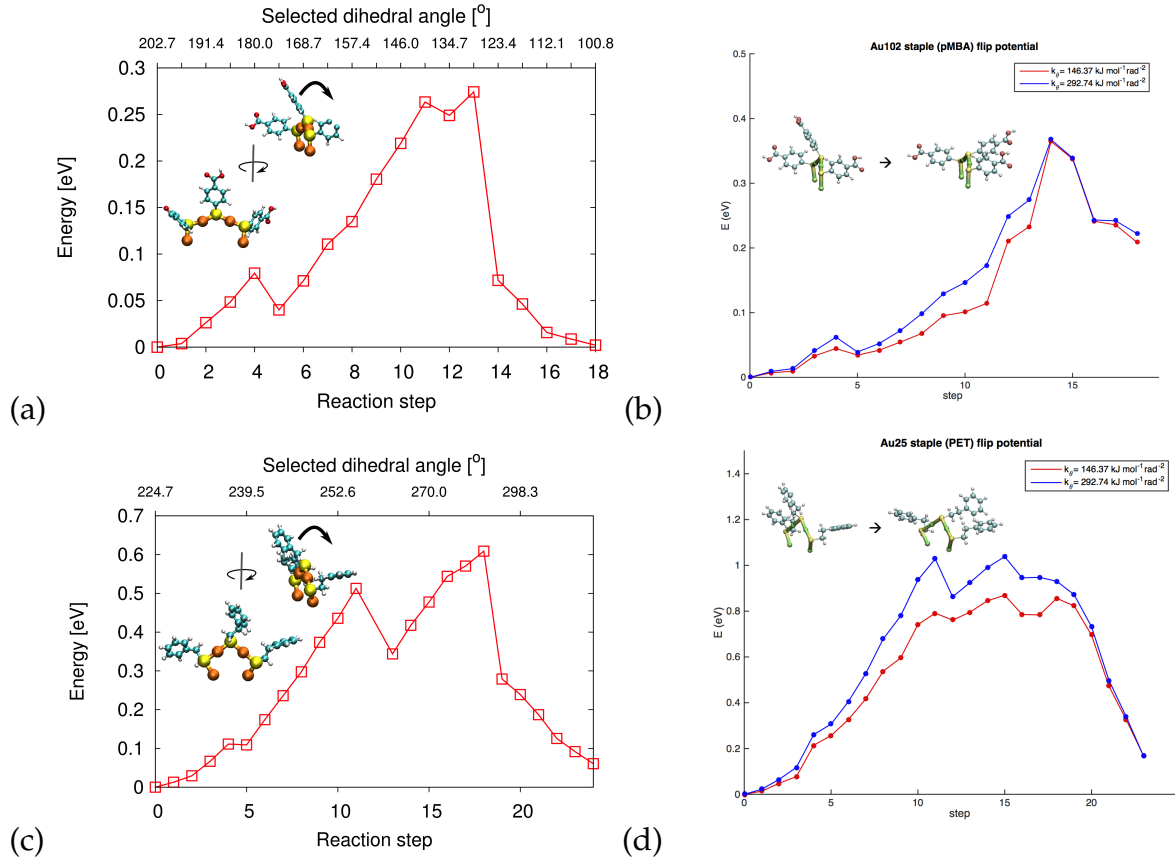


Figure 8: Ligand flipping energy barriers from constrained relaxation DFT and MD.

Constrained relaxation DFT predicts barriers of around 0.3 eV and 0.6 eV for the central ligand flipping in the Au₁₀₂ and Au₂₅ staples, respectively. Corresponding barriers in MD are around 0.4 eV and 0.9 eV. The barriers in MD are therefore to some extent larger than those predicted by DFT, yet in the same order of magnitude. A crude MD simulation for the flipping al[] in the staple form present in Au₁₄₄ cluster was tested, predicting barrier around 0.6 eV. Due to relatively low barriers, flipping in the room temperature could be expected for all these clusters. Hence an additional chirality flip restrictive potential may not be needed for the MD simulations. []

MD/DFT simulations

The dynamics and structural changes of the $\text{Au}_{25}(\text{PET})_{18}^-$ cluster were studied in picosecond time scale in vacuum with MD/DFT simulations and compared to classical MD simulations. Structural changes were studied by examining distributions of atomic distances and angles in different simulations, presented in figures 9 and 10.

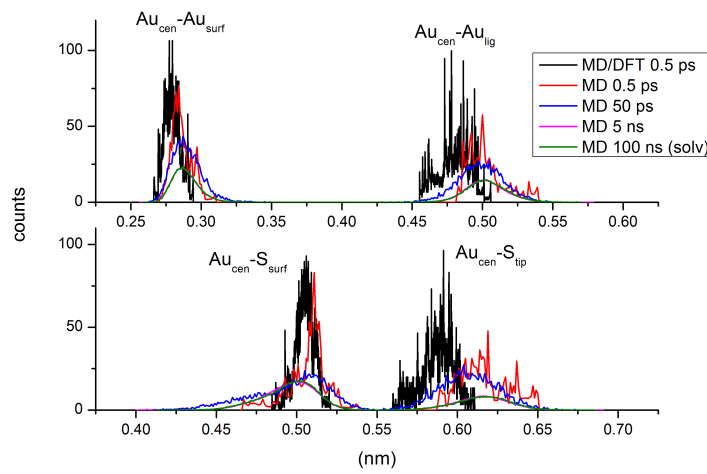


Figure 9: Distirbution of atom distances from the central Au atom.

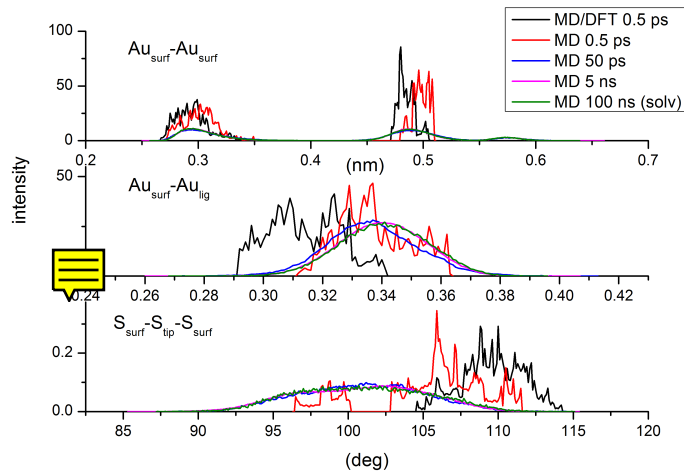


Figure 10: Bond and angle distributions.

Expectedly, the distribution of distances and angle broadens with increasing simulation time. Comparing the the MD/DFT simulation and MD simulation of equal time (0.5 ps), the distributions differ to some extent, generally so that the distributions appear wider in the MD simulation. These differences could be related to variations in the starting structures and simulation propagation and equilibration between MD and MD/DFT.

In comparing the average values for distances, those observed in the MD simulations are on average to some extent larger than the ones in MD/DFT. These differences could be due to variations in the structures that are not smeared out during the very short simulation time. The averages shift also in comparing between MD simulations of different simulation times, evening out the gap between MD and MD/DFT. For the reported angle a decreasing trend can be observed in going from MD/DFT to MD. The fluctuations of different atom positions in general expectedly increase with the simulation time. The fluctuations appeared minutely larger in MD compared to MD/DFT in the same time scale.

Comparing the distance and angle distributions to longer MD/DFT simulation (10 ps) for $\text{Au}_{25}\text{H}_{18}^-$ presented in⁴², there appear no drastic differences in the observed distance and angle ranges. Especially, the ranges of the reported distances and angle appearing in the longer time scale MD simulations do not exceed those observed already in 10 ps MD/DFT. Mean square displacements reported in⁴² also qualitatively agree to those observed in this work for similar time scale. The peak positions or averages for bond distances qualitatively agree as well between MD and MD/DFT. The most emphasized difference appears again in the $S_{\text{surf}} - S_{\text{tip}} - S_{\text{surf}}$ angle, which on average for MD appears clearly smaller compared to MD/DFT.

In conclusion, based on the reported distances the structural changes in the cluster do not drastically differ between MD simulation compared to MD/DFT scheme. However, the short simulation at MD/DFT does not visually appear to caption the distortion of the staples observed in the longer time scale MD simulations, which could be reflected, e.g,

in the observed distributional difference in the $S_{\text{surf}} - S_{\text{tip}} - S_{\text{surf}}$ angle between MD and MD/DFT. In spite of the folding, the range of the observed angles and distances agree between 10 ps MD/DFT and MD also at longer MD time scales, indicating therefore no severe distortions in the structures.

Conclusion and outlook

AMBER force field parameters for 5 different gold nanoclusters were constructed and tested in MD simulations in 100 ns time scale. For justification of the parameters, comparisons against available experimental data along with DFT calculations and previous results were made. The test simulations in solvents up to time scale of 100 ns for each cluster showed that the symmetry of the gold core is stable in all clusters in simulations at room temperature. The rectangular staple structures were also well retained. The V-shaped staples in the $\text{Au}_{25}(\text{PET})_{18}$ cluster exhibited more folding and visual distortion, but the gold framework retained the shape in spite of the staple folding. In general, smaller clusters exhibited larger deviations in the overall structure reflecting the larger folding space for the ligands.

Comparison to the experimental data was addressed via diffusion coefficients and an experimental crystal structure. The calculated diffusion coefficients qualitatively reproduced the experimental results. The observed differences could be related to insufficient statistics and differences in cluster or solvent parameters. The agreement between diffusion coefficients also indicates similarity in the hydrodynamic radii of the clusters, and hence correct tendency of folding the ligand shell in the simulation. For the crystal simulation of $\text{Au}_{102}(\text{pMBA})_{44}$ cluster the experimental crystal structure was relatively well retained in the simulation mimicking crystallization conditions, indicating no drastic problems in the cluster parameters. In addition, simulations in different solvent conditions were clearly less successful in maintaining of the experimental crystal structure, and in that sense the

simulation was capable of reproducing a correct course towards the experimental result.

Comparisons to the DFT results were made against energy barriers of ligand flipping and MD/DFT simulations. The ligand flipping barriers appeared higher in the MD compared to DFT, yet in the same order of magnitude. Due to relatively low barriers, ligand flipping may be expected in simulations at room temperature. Therefore, the use of separate flipping restricting potential utilized in this work may not be necessary. Comparisons to MD/DFT simulations showed small differences in distribution of atomic distances and more emphasized difference was observed for the angle between sulfurs in the staple of the $\text{Au}_{25}(\text{PET})_{18}$ cluster. Despite the differences in the average values, the ranges of the observed distances and angle are similar between 10 ps MD/DFT and even the long time scale MD (100 ns in solvent), suggesting no drastic differences in the capability of evolving of the structure.

The current results suggest that the parameter set adopted here can be generally applied to perform stable MD simulations of various sized symmetric gold clusters with different ligands and in different solvents within AMBER force field. Qualitative reproduction of available experimental results have provided some further justification for these parameters. All the clusters studied in this work are symmetric considering the gold core, and applying these parameters for less symmetric cluster structures, such as Au_{11} and Au_{13} , is yet to be addressed. The use of 0 charged Au atoms may not be justified in all systems and e.g., RESP fitting could be utilized to assign charges for the Au atoms as well. Also, for the purposes of these simulations the optimal protonation state of the pMBA ligated clusters were not considered. Optimization of the ligand protonation states⁴³ at specific pH will be crucial in future simulations with cluster combined, e.g., with biomolecules. The calculation of these protonation states is currently underway.

The availability of simulating different sized gold clusters in a biologically oriented classical force field could provide further means for computational studies of biological systems, such as viruses or other proteins, conjugated with these clusters. In addition,

MD simulations of different types of cluster systems could also aid in providing, e.g., representative structures for DFT or other higher level calculations, possibly for more complicated cluster systems as well.

References

- (1) Häkkinen, H. *Nature Chemistry* **2012**, *4*, 443–455.
- (2) Heinz, H.; Vaia, R. A.; Farmer, B. L.; Naik, R. R. *J. Phys. Chem. C* **2008**, *112*, 17281–17290.
- (3) Leng, Y.; Krstić, P. S.; Wells, J. C.; Cummings, P. T.; Dean, D. J. *The Journal of Chemical Physics* **2005**, *122*, –.
- (4) Van Lehn, R. C.; Alexander-Katz, A. *The Journal of Physical Chemistry C* **2013**, *117*, 20104–20115.
- (5) Van Lehn, R. C.; Alexander-Katz, A. *The Journal of Physical Chemistry B* **2014**, *118*, 12586–12598, PMID: 25347475.
- (6) Van Lehn, R. C.; Ricci, M.; Silva, P. H. J.; Andreozzi, P.; Reguera, J.; Voitchovsky, K.; Stellacci, F.; Alexander-Katz, A. *Nature communications* **2014**, *5*, 4482.
- (7) Heikkilä, E.; Gurtovenko, A. A.; Martinez-Seara, H.; Häkkinen, H.; Vattulainen, I.; Akola, J. *The Journal of Physical Chemistry C* **2012**, *116*, 9805–9815.
- (8) Heikkilä, E.; Martinez-Seara, H.; Gurtovenko, A. A.; Vattulainen, I.; Akola, J. *Biochimica et Biophysica Acta (BBA) - Biomembranes* **2014**, *1838*, 2852 – 2860.
- (9) Verde, A. V.; Acres, J. M.; Maranas, J. K. *Biomacromolecules* **2009**, *10*, 2118–2128, PMID: 19621884.
- (10) Lee, K. H.; Ytreberg, F. M. *Entropy* **2012**, *14*, 630–641.

- (11) Ramezani, F.; Habibi, M.; Rafii-Tabar, H.; Amanlou, M. *DARU Journal of Pharmaceutical Sciences* **2015**, 23.
- (12) Kokh, D. B.; Corni, S.; Winn, P. J.; Hoefling, M.; Gottschalk, K. E.; Wade, R. C. *Journal of Chemical Theory and Computation* **2010**, 6, 1753–1768.
- (13) KRUPA, P.; MOZOLEWSKA, M. A.; RASULEV, B.; CZAPLEWSKI, C.; LESZCZYNSKI, J. *TASK QUARTERLY* **2014**, 18, 337–341.
- (14) Alsharif, S. A.; Chen, L. Y.; Tlahuice-Flores, A.; Whetten, R. L.; Yacaman, M. J. *Phys. Chem. Chem. Phys.* **2014**, 16, 3909–3913.
- (15) Lal, M.; Plummer, M.; Purton, J.; Smith, W. *Proceedings of the Royal Society of London A: Mathematical, Physical and Engineering Sciences* **2011**, 467, 1986–2003.
- (16) Antúnez-García, J.; Mejía-Rosales, S.; Pérez-Tijerina, E.; Montejano-Carrizales, J. M.; José-Yacamán, M. *Materials* **2011**, 4, 368–379.
- (17) Böyükata, M. *Physica E: Low-dimensional Systems and Nanostructures* **2006**, 33, 182 – 190.
- (18) Erkoç, Ş. *Physica E: Low-dimensional Systems and Nanostructures* **2000**, 8, 210 – 218.
- (19) Mariscal, M. M.; Olmos-Asar, J. A.; Gutierrez-Wing, C.; Mayoral, A.; Yacaman, M. J. *Phys. Chem. Chem. Phys.* **2010**, 12, 11785–11790.
- (20) Legenski, N.; Zhou, C.; Zhang, Q.; Han, B.; Wu, J.; Chen, L.; Cheng, H.; Forrey, R. C. *Journal of Computational Chemistry* **2011**, 32, 1711–1720.
- (21) Fihey, A.; Maurel, F.; Perrier, A. *Phys. Chem. Chem. Phys.* **2014**, 16, 26240–26251.
- (22) Keith, J. A.; Fantauzzi, D.; Jacob, T.; van Duin, A. C. T. *Phys. Rev. B* **2010**, 81, 235404.
- (23) Järvi, T. T.; van Duin, A. C. T.; Nordlund, K.; Goddard, W. A. *The Journal of Physical Chemistry A* **2011**, 115, 10315–10322, PMID: 21780819.

- (24) Bae, G.-T.; Aikens, C. M. *The Journal of Physical Chemistry A* **2013**, *117*, 10438–10446, PMID: 24041237.
- (25) Banerjee, S.; Montgomery, J.; Gascón, J. *Journal of Materials Science* **2012**, *47*, 7686–7692.
- (26) Marjomäki, V.; Lahtinen, T.; Martikainen, M.; Koivisto, J.; Malola, S.; Salorinne, K.; Pettersson, M.; Häkkinen, H. *Proceedings of the National Academy of Sciences* **2014**, *111*, 1277–1281.
- (27) Hess, B.; Kutzner, C.; van der Spoel, D.; Lindahl, E. *Journal of Chemical Theory and Computation* **2008**, *4*, 435–447.
- (28) Lindorff-Larsen, K.; Piana, S.; Palmo, K.; Maragakis, P.; Klepeis, J. L.; Dror, R. O.; Shaw, D. E. *Proteins: Structure, Function, and Bioinformatics* **2010**, *78*, 1950–1958.
- (29) Henkelman, G.; Arnaldsson, A.; Jónsson, H. *Computational Materials Science* **2006**, *36*, 354 – 360.
- (30) Sanville, E.; Kenny, S. D.; Smith, R.; Henkelman, G. *Journal of Computational Chemistry* **2007**, *28*, 899–908.
- (31) Tang, W.; Sanville, E.; Henkelman, G. *Journal of Physics: Condensed Matter* **2009**, *21*, 084204.
- (32) Bayly, C. I.; Cieplak, P.; Cornell, W.; Kollman, P. A. *The Journal of Physical Chemistry* **1993**, *97*, 10269–10280.
- (33) Case, D. A. et al. AMBER 12. 2012; <http://ambermd.org/>.
- (34) Frisch, M. J. et al. Gaussian09 Revision D.01. Gaussian Inc. Wallingford CT 2009.
- (35) Weigend, F. *Phys. Chem. Chem. Phys.* **2006**, *8*, 1057–1065.
- (36) Wang, J.; Wolf, R. M.; Caldwell, J. W.; Kollman, P. A.; Case, D. A. *Journal of Computational Chemistry* **2004**, *25*, 1157–1174.

- (37) Caleman, C.; van Maaren, P. J.; Hong, M.; Hub, J. S.; Costa, L. T.; van der Spoel, D. *Journal of Chemical Theory and Computation* **2012**, *8*, 61–74, PMID: 22241968.
- (38) van der Spoel, D.; van Maaren, P. J.; Caleman, C. *Bioinformatics* **2012**, *28*, 752–753.
- (39) Salorinne, K.; Lahtinen, T.; Koivisto, J.; Kalenius, E.; Nissinen, M.; Pettersson, M.; Häkkinen, H. *Analytical Chemistry* **2013**, *85*, 3489–3492, PMID: 23506040.
- (40) Wang, J.; Hou, T. *Journal of Computational Chemistry* **2011**, *32*, 3505–3519.
- (41) Jadzinsky, P. D.; Calero, G.; Ackerson, C. J.; Bushnell, D. A.; Kornberg, R. D. *Science* **2007**, *318*, 430–433.
- (42) Mäkinen, V.; Häkkinen, H. *The European Physical Journal D* **2012**, *66*.
- (43) Donnini, S.; Tegeler, F.; Groenhof, G.; Grubmüller, H. *Journal of Chemical Theory and Computation* **2011**, *7*, 1962–1978.